LA-UR-24-24644
Accepted Manuscript

Anisotropic heating and parallel heat flux in electron-only magnetic reconnection with intense guide fields

Ren, Jincai
Arro, Giuseppe
Innocenti, Maria Elena
Lapenta, Giovanni

To be published in: Journal of Plasma Physics

DOI to publisher's version: 10.1017/S0022377825100548

Permalink to record:
https://permalink.lanl.gov/object/view?what=info:lanl-repo/lareport/LA-UR-24-24644

J. Plasma Phys. (2025), *vol.* 91, E105

doi:10.1017/S0022377825100548

Anisotropic heating and parallel heat flux in electron-only magnetic reconnection with intense guide fields

Jincai Ren[1], **Giuseppe Arrò**[2], **Maria Elena Innocenti**[3] and **Giovanni Lapenta**[1]

[1]Department of Mathematics, KU Leuven, Celestijnenlaan 200B, Leuven 3001, Belgium
[2]Los Alamos National Laboratory, Theoretical Division, Los Alamos, NM 87545, USA
[3]Institut für Theoretische Physik, Ruhr-Universität Bochum, 44801 Bochum, Germany

Corresponding author: Jincai Ren, jincairen.physics@gmail.com

(Received 6 February 2025; revision received 3 June 2025; accepted 4 June 2025)

Electron-only reconnection (E-REC) is a process recently observed in the Earth’s magnetosheath, where magnetic reconnection occurs at electron kinetic scales, and ions do not couple to the reconnection process. Electron-only reconnection is likely to have a significant impact on the energy conversion and dissipation of turbulence cascades at kinetic scales in some settings. This paper investigates E-REC under different intensities of strong guide fields (the ratio between the guide field and the in-plane asymptotic field strength is 5, 10 and 20, respectively) via two-dimensional fully kinetic particle-in-cell simulations, focusing on electron heating. The simulations are initialized with a force-free current sheet equilibrium under various intensities of strong guide fields. Similarly to previous experimental studies, electron temperature anisotropy along separatrices is observed, which is found to be mainly caused by the variations of parallel temperature. Both regions of anisotropy and parallel temperature increase/decrease along separatrices become thinner with increasing guide fields. Besides, we find a transition from a quadrupolar to a hexapolar (six-polar) to an octopolar (eight-polar) structure in temperature anisotropy and parallel temperature as the guide field intensifies. Non-Maxwellian electron velocity distribution functions (EVDFs) at different locations in the three simulations are observed. Our results show that parallel electron velocity varies notably with different guide field intensities and finite parallel electron heat flux density is observed. The three simulations exhibit features of the Chew–Goldberger–Low theory, with the level of consistency increasing as the guide field strength increases. This explains the electron parallel temperature variations and the shape of the EVDFs observed along the separatrices. This work may provide insights into the understanding of electron heating and parallel heat flux density in E-REC observed in the turbulent magnetosheath.

Key words: space plasma physics, plasma heating, plasma simulation

1. Introduction

Magnetic reconnection is a ubiquitous phenomenon observed in space, fusion and laboratory plasmas. During this process, the magnetic field topology is modified and magnetic energy is converted into plasma kinetic and thermal energy (Biskamp 2000; Birn & Priest 2007; Hesse & Cassak 2020; Ji *et al*. 2023; Lu *et al*. 2023). Throughout the past decades, the standard ion-scale magnetic reconnection has been studied extensively through laboratory experiments, spacecraft observations, theoretical analysis and numerical simulations, and significant progress has been made within this domain (Innocenti *et al*. 2015; Hesse & Cassak 2020; Ji *et al*. 2023). The term 'standard ion-coupled magnetic reconnection' here refers to a reconnection regime in which both ions and electrons are involved. Such reconnection processes take place in current sheets of size typically larger than ion scales and imply the transfer of energy from magnetic fields to both ions and electrons. As a result, both ions and electrons are accelerated out of the reconnection region, with each species displaying rapid outflow jets moving in opposite directions (Zweibel & Yamada 2009).

On the other hand, a novel regime of magnetic reconnection, dubbed electron-only reconnection (E-REC), has been observed at scales smaller than ion scales, and ions do not couple to this process. Thanks to the advancement of spacecraft *in situ* diagnostics with unprecedented high resolution, E-REC has been observed in the Earth's magnetosheath by Phan *et al*. (2018) for the first time. Given the tiny spatial and temporal scales characterizing E-REC, ions are unable to respond to the small-scale magnetic field dynamics and thus ion outflow jets existing in standard ion-coupled reconnection are absent in E-REC (Sharma Pyakurel *et al*. 2019; Arrò *et al*., 2020; Califano *et al*. 2020; Lu *et al*. 2020, 2022; Hubbert *et al*. 2022; Shi *et al*. 2022*a*,*b*; Guan *et al*. 2023; Shi *et al*. 2023; Roy *et al*. 2024). Differently from its ion-scale counterpart, E-REC does not exhibit oppositely directed ion jets out of the reconnection region, and only electron outflows are observed. Furthermore, the thickness of the associated current sheet is of the order of the electron inertial length d_e and the electron outflow speed is super-Alfvénic (Phan *et al*. 2018).

Electron-scale current sheets connected with E-REC have been observed in satellite measurements and numerical simulations of turbulence and large-scale reconnection (Phan *et al*. 2018; Stawarz *et al*. 2019, 2022; Arrò *et al*., 2020), and they are likely to have a significant impact on the energy conversion and dissipation within turbulence environments in some settings like the magnetosheath of Earth (Arrò *et al*., 2020; Califano *et al*. 2020; Franci *et al*. 2022). It has been demonstrated that E-REC also develops as a secondary effect in the outflows of large-scale three-dimensional (3-D) reconnection (Lapenta *et al*. 2015, 2022), a phenomenon which has been confirmed by spacecraft observations (Zhong *et al*. 2021). Sharma Pyakurel *et al*. (2019) studied the transition from ion-coupled reconnection to E-REC under conditions of plasma beta greater than one and strong guide fields ($B_g = 8B_{x0}$; hereafter B_g and B_{x0} represent the strength of the guide field and in-plane asymptotic reconnecting field, respectively). Califano *et al*. (2020) and Arrò *et al*. (2020) investigated the formation and roles of E-REC in plasma turbulence and analysed the statistical properties of turbulent fluctuations in both the E-REC and the standard ion-coupled reconnection regimes. However, the particle heating in E-REC is still not comprehensively understood.

Remarkable progress has been made in understanding two-dimensional (2-D) antiparallel reconnection over the past decades. Here, antiparallel reconnection refers to a configuration in which two regions with oppositely directed magnetic fields are present in a plane and the out-of-plane component of the upstream magnetic fields (i.e. the guide field) is zero. In this case, reconnection happens at the neutral sheet between the oppositely directed magnetic fields. It has been shown that the addition of the out-of-plane guide field alters the reconnection process dramatically, even when the guide field is small in magnitude. The presence of guide fields influences the reconnection rate, modifies the structure of diffusion region and affects particle motion (Ricci *et al*. 2004; Swisdak *et al*. 2005; Hesse 2006; Birn & Priest 2007; Stanier *et al*. 2015*a*,*b*; Muñoz & Büchner 2016; Wilson *et al*. 2016; Granier *et al*. 2024). Some studies have found that the guide field decreases the reconnection rate (Muñoz & Büchner 2016; Wilson *et al*. 2016), while others report little influence (Hesse *et al*. 1999; Pritchett 2001) or even an enhancement under certain conditions (Stanier *et al*. 2017; Xiong *et al*. 2024). A density asymmetry is typically observed along separatrices in guide field reconnection (Kleva *et al*. 1995; Rogers *et al*. 2003; Pritchett 2005; Birn & Priest 2007; Lapenta *et al*. 2011; Markidis *et al*. 2012). Usually, the density is enhanced on one separatrix but is reduced along the other. Besides, the reconnection current sheet typically tilts (Birn & Priest 2007). Consistent with the quadrupolar field configuration predicted by the Hall-reconnection model, a quadrupolar out-of-plane magnetic field perturbation generated by the in-plane electron current is observed in guide field reconnection (Pritchett 2005). Furthermore, tripolar magnetic field structures have also been reported in Newman, Eriksson & Lapenta (2022). The guide field is also found to have a remarkable impact on the location of energy transfer and particle dynamics, including increasing the electron energy gain and affecting the electron heating in the diffusion region (Guo *et al*. 2015; Yi *et al*. 2020). Up to now, the majority of guide field reconnection research has been focusing on the ion-coupled regime, typically involving weak or moderate strength guide fields (Horiuchi, Usami & Ohtan 2014; McCubbin, Howes & TenBarge 2022) (Here we regard the guide field with strength of $B_g/B_{x0} < 5$ as weak or moderate and the guide field with strength of $B_g/B_{x0} \geqslant 5$ as intense/strong). Electron-only reconnection in the presence of intense guide fields has not been thoroughly explored numerically, except for notable contributions by Sharma Pyakurel *et al*. (2019), Mallet (2020), Guan *et al*. (2023) and Roy *et al*. (2024). Sharma Pyakurel *et al*. (2019) and Guan *et al*. (2023) studied the transition between E-REC and standard ion-coupled reconnection with strong guide fields and found that the simulation domain size and ion cyclotron radius ρ_i are two key parameters for this transition. Mallet (2020) studied the onset of E-REC and proposed the 'collapsE-REConnection' explanation for E-REC in low-β collisionless plasmas. More recently, Roy *et al*. (2024) compared and analysed the energy dissipation in the E-REC and standard ion-coupled reconnection through the combination of observations and 2.5-dimensional (2.5-D) particle-in-cell (PIC) simulations.

The energy transfer between the electromagnetic fields and plasma influences both the kinetic and thermal energy of electrons during magnetic reconnection (Yang *et al*. 2017*a*,*b*). Pucci *et al*. (2018) studied parallel and perpendicular heating in guide field reconnection with B_g/B_{x0} ranging from 0 to 3 through 2.5-D Particle-in-Cell (PIC) simulations. More recently, Shi *et al*. (2023) has shown evidence of temperature anisotropy developing along separatrices in E-REC experiments with strong guide fields ($B_g/B_{x0} = 25$), conducted in the context of the PHASMA (phase space mapping facility) experiment (Shi *et al*. 2021). Their investigation suggests that the observed anisotropy arises from parallel electric field heating rather than by Fermi or betatron acceleration. The anisotropy along the separatrices appearing in the PHASMA experiment exhibits a different pattern with respect to the anisotropy observed in previous small-scale reconnection simulations (Pucci *et al.* 2018), an effect probably caused by the non-negligible Coulomb collisions taking place in the PHASMA experiment (Shi *et al.* 2023). However, the role of strong guide fields in influencing temperature anisotropy in E-REC has been poorly investigated from a numerical point of view.

Non-Maxwellian electron velocity distribution functions (EVDFs) have been observed in both simulations (Ng *et al.* 2011; Muñoz *et al.* 2014; Shuster *et al.* 2015; Muñoz & Büchner 2016; Shay *et al.* 2016) and satellite observations (Burch *et al.* 2016; Lapenta *et al.* 2017*a*; Zhou *et al.* 2019) of standard ion-coupled magnetic reconnection. Egedal *et al.* (2008) and Egedal *et al.* (2013), the authors developed a trapping model to explain the acceleration and the temperature anisotropy typically observed in guide field reconnection, which has been validated by both spacecraft observations and numerical simulations. On the contrary, the kinetic features of E-REC are still poorly explored and the only experimental evidence for non-Maxwellian EVDFs comes from the PHASMA experiments (Shi *et al.* 2022*a*,*b*, 2023).

In this work, we analyse three numerical simulations of E-REC with varying intense guide field strengths ($B_g/B_{x0} = 5$, 10 and 20, respectively), focusing on electron heating. The quadrupolar structures of the out-of-plane magnetic field variations are shown. Similarly to standard ion-coupled reconnection (Pritchett & Coroniti 2004), we find asymmetric density structures for electrons in E-REC. Electron outflow speeds are super-Alfvénic and ion outflow jets are absent, which is the characteristic feature of the E-REC (Phan *et al.* 2018). We also find that the increase of guide fields leads to the thinning of both the quadrupolar structure of the out-of-plane magnetic field and the asymmetric structure of density (Kleva *et al.* 1995; Birn & Priest 2007). Electron temperature anisotropy along separatrices is observed in our E-REC simulations. Perpendicular temperature increase is found along one separatrix, while perpendicular temperature decreases along the other. Parallel temperature increase/decrease, on the other hand, is much stronger than perpendicular temperature variations and plays a major role in the anisotropy. Parallel temperature increase is on one separatrix, while parallel temperature decrease distributes along the other. Both regions of the anisotropy and parallel temperature increase/decrease along separatrices become narrower as the guide field intensifies. Moreover, the strength of guide fields has notable effects on the parallel temperature in the outflow regions. We find a transition from a quadrupolar to a hexapolar to an octopolar structure in temperature anisotropy and parallel temperature as the guide field increases. We further analyse the non-Maxwellian EVDFs at different locations, especially regions with strong anisotropy. Our results show that the EVDFs are close to gyrotropic, though small finite agyrotropy is observed. Moreover, parallel electron speed varies notably with different guide field intensities and finite parallel electron heat flux density is observed. Our analyses indicate that our three simulations exhibit features of the Chew–Goldberger–Low (CGL) theory. As the guide field strength increases, the simulations show a progressively stronger alignment with the CGL theory predictions.

2. Simulation set-up

The simulations are carried out in a 2-D geometry using the fully kinetic semi-implicit PIC code ECsim (Lapenta 2017; Gonzalez-Herrero, Boella & Lapenta 2018), which has been extensively used to simulate magnetic reconnection

(Lapenta *et al.* 2017*b*), plasma turbulence (Arrò *et al.* 2022), fusion tokamak dynamics (Ren & Lapenta 2024) and in solar wind instabilities (Micera *et al.* 2020). Given the low plasma β, we initialize our simulations with a force-free current sheet equilibrium, which is unstable to the plasmoid instability and is widely utilized in E-REC simulations (Pyakurel *et al.* 2021; Guan *et al.* 2023). In our set-up, x is the asymptotic direction of the in-plane magnetic field, y is the direction across the sheets and z is the out-of-plane direction. The ratio between ion and electron inertial length is $d_i/d_e = 10$ (d_i and d_e are ion inertial length and electron inertial length, respectively). The simulation domain is a square box whose size is $L_x \times L_y = 20d_e \times 20d_e = 2d_i \times 2d_i$. The x component of the initial magnetic field profile is given by

$$B_x(y) = B_{x0}\left[\tanh\left(\frac{y-y_1}{\delta_1}\right) - \tanh\left(\frac{y-y_2}{\delta_2}\right) - 1\right]. \tag{2.1}$$

Here y_1 and y_2 represent the location of the two current sheets, with $y_1 = L_y/4$, $y_2 = 3L_y/4$. Here δ_1 and δ_2 are the thickness of the current sheet at $y = y_1$ and $y = y_2$, respectively. Here $B_{x0} = 0.002$. The thicknesses of the two current sheets are $\delta_1 = 0.1d_i = 1d_e$ and $\delta_2 = 0.05d_i = 0.5d_e$ so both sheets are at electron kinetic scales. We find the evolution of reconnection in these two sheets has similar patterns except that the thinner (upper) sheet evolves faster, as expected (Zelenyi & Krasnoselskikh 1979). We choose the upper sheet for the analysis and its evolution remains unaffected by the lower sheet, as the latter exhibits a slower development. The out-of-plane magnetic field B_z is given by

$$B_z(y) = \left[B_g^2 + B_{x0}^2 - B_x^2(y)\right]^{1/2}, \tag{2.2}$$

with B_g denoting the asymptotic guide field, far from the current sheet. This magnetic field configuration implies a force-free equilibrium in 2-D geometry. All three simulations are conducted with the same parameters, except for the asymptotic guide field strength B_g. It is chosen to be $B_g = 0.01 = 5B_{x0}$ for simulation A, $B_g = 0.02 = 10B_{x0}$ for simulation B and $B_g = 0.04 = 20B_{x0}$ for simulation C. These strengths are typically observed in the Earth's magnetosheath (Stawarz *et al.* 2022). The initial current is calculated from Ampère's law (without displacement current) and all currents are carried by electrons. The thermal velocities of electrons and ions are $v_{th,e} = 0.05\,c$ and $v_{th,i} = 0.002\,c$, respectively (c is the speed of light). We do not add perturbations to our simulations, and reconnection, in such thin current sheets, starts as a plasmoid instability triggered by the numerical noise (Pritchett 2005; Newman *et al.* 2022).

The simulation box is discretized with a mesh of 512×512 cells. The grid step is approximately $\Delta x = \Delta y \simeq 0.04d_e$. Both the electron gyroradius and electron inertial length are resolved with this spatial resolution for all cases. Table 1 shows the cyclotron radius for electrons (ρ_e) and ions (ρ_i), as well as the plasma β for electrons (β_e) and ions (β_i) in three simulations. These β values correspond to a temperature ratio of $T_e/T_i = 6.25$ due to using a reduced (but still quite high) mass ratio $m_i/m_e = 100$ in all three simulations. The time step is $\mathrm{d}t = 0.01\omega_{ce}^{-1}$, $0.02\omega_{ce}^{-1}$, $0.04\omega_{ce}^{-1}$ (ω_{ce} is electron cyclotron frequency) in the three simulations, respectively, resolving the electron cyclotron motion in all simulations. The number of particles per cell is 8192 for each species. Periodic boundary conditions are considered in all directions. Particles are initialized from Maxwellian distributions. The density is uniform and is set to be unity for both species and quasineutrality is initially satisfied. The ratios

	$B_g = 5B_{x0}$	$B_g = 10B_{x0}$	$B_g = 20B_{x0}$
ρ_e/d_e	0.490	0.249	0.125
ρ_i/d_e	1.961	0.995	0.499
β_e	0.481	0.124	0.031
β_i	0.077	0.020	0.005

TABLE 1. Cyclotron radius for electrons (ρ_e) and ions (ρ_i), plasma β for electrons (β_e) and ions (β_i) in the three simulations under investigation.

between the electron plasma frequency (ω_{pe}) and the electron cyclotron frequency (ω_{ce}) are 10, 5 and 2.5 in simulations A, B and C, respectively.

3. Results

In this section, we outline the key findings of our simulations. Section 3.1 details the evolution of reconnected flux, reconnection rate and the reconnection structure. These results align qualitatively with previous findings, providing a contextual foundation for the subsequent analyses. Sections 3.2 and 3.3 present the results pertaining to electron anisotropic heating and the EVDFs, which represent novel contributions to this field.

3.1. *Reconnection rate and structure*

The reconnected flux and reconnection rate of simulation A are shown in figure 1(*a*). The reconnected flux Ψ is computed as the difference between the maximum and minimum of the out-of-plane component of vector potential A_z along the upper current sheet. The reconnection rate E_r is calculated as $E_r = \partial\Psi/\partial t$ and is normalized by the in-plane asymptotic magnetic field B_0 and the inflow Alfvén speed $V_A = B_0/\sqrt{\mu_0\rho}$. We find that reconnection goes through a slow 'build-up' phase at first and this lasts until approximately $t = 80\omega_{ce}^{-1}$. Then the reconnection rate increases steadily and reaches the first peak at $t = 265\omega_{ce}^{-1}$. Afterwards, it decreases first and later returns to increasing from $t = 380\omega_{ce}^{-1}$, which is caused by the coalescence of magnetic islands. A second peak is then reached, followed by a new decrease. It is noted that the first peak rate is larger. In our simulations, due to the relatively small size of the box in the y direction, the lack of 'fresh' plasma to process in the reconnection region prevents reaching and maintaining the steady-state (Wan & Lapenta 2008).

The reconnected flux and reconnection rate of simulations B and C are illustrated in figure 1(*b,c*), respectively. They have similar patterns as case A. The reconnection is very slow initially, and then after the 'build-up' phase, both the reconnected flux and the reconnection rate increase gradually. Then the rate reaches a peak value and decreases later while the reconnected flux still increases. However, cases B and C do not exhibit a second peak, unlike case A. This is because simulations B and C are not run to the point where magnetic islands coalesce. The coalescence does not affect our results since we carry out the analysis at an earlier time (as shown below). We find that the reconnection is delayed with large guide fields due to reducing electron gyroradius. The reconnection rate starts to increase from $t \approx 100\omega_{ce}^{-1}$ in case A, $t \approx 300\omega_{ce}^{-1}$ in case B and $t \approx 1000\omega_{ce}^{-1}$ in case C, respectively. This is because when

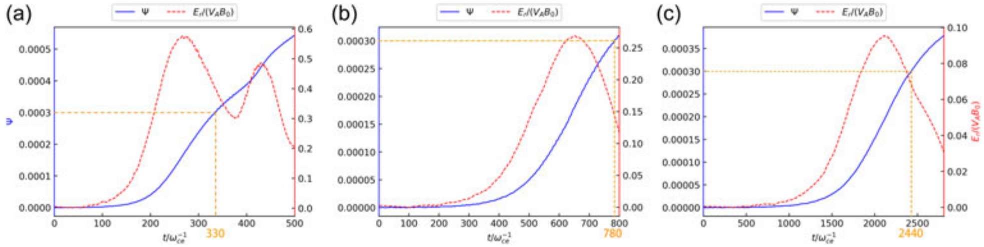

FIGURE 1. Reconnected flux and reconnection rate in the three cases: (*a*) case A ($B_g = 5B_{x0}$); (*b*) case B ($B_g = 10B_{x0}$); (*c*) case C ($B_g = 20B_{x0}$). The orange dashed lines represent the time snapshots used to compare the three simulations. These three snapshots have the same reconnected flux and roughly the same island size. The reconnection rate E_r is normalized by the inflow Alfvén speed V_A and in-plane asymptotic magnetic field B_0.

the guide field increases, the ratio between the initial current sheet thickness (which is kept fixed in our simulations) and the electron gyroradius becomes larger and it takes longer for the sheet to become narrow enough and for the field lines to reconnect, as pointed out by Shay *et al.* (2004). Furthermore, it is noted that the maximum reconnection rate decreases when the guide field increases (to compare the reconnection rate, as done in Ng *et al.* (2015), Stanier *et al.* (2017) and Guan *et al.* (2023), we use the maximum reconnection rate here since our simulations do not reach a steady state). These results suggest that large guide fields delay the onset of reconnection and decrease the maximum reconnection rate, which is analogous to previous ion-coupled reconnection works (Hesse *et al.* 2002; Ricci *et al.* 2004; Muñoz & Büchner, 2016). In the following sections, we will analyse and compare the three simulations when the plasmoid instability is well-developed. The times chosen for the comparison are indicated by the orange dashed lines in figure 1, and we select those times because they correspond to the same reconnected flux. Since the reconnected flux is a measure of the islands' size, the islands at these three times have roughly the same size.

In figure 2(*a*–*c*), we compare the out-of-plane magnetic field variations $\delta B_z = B_z(t) - B_z(t=0)$ of the three runs at the times indicated in figure 1. Here, $B_z(t)$ denotes the out-of-plane magnetic field at time t (so $B_z(t=0)$ represents the initial out-of-plane magnetic field). Solid lines represent the in-plane component of magnetic field lines and we notice the presence of a well-developed reconnection region in all three runs, with magnetic islands of comparable size. We find that B_z increases along the separatrix in the upper left-hand and lower right-hand quadrants (where $\delta B_z > 0$), whereas it decreases along the other separatrix in the upper right-hand and lower left-hand quadrants (where $\delta B_z < 0$). This result is the same as the quadrupolar structure in the Hall reconnection model (Zweibel & Yamada 2009; Muñoz Sepúlveda 2015) and is consistent with Sharma Pyakurel *et al.* (2019). It is noted that the perturbation is relatively small and would not change the sign of the total out-of-plane magnetic field. In addition, we also find the structure of δB_z varies as the guide field increases. In case A, δB_z is less localized, exhibiting wide spatial variations, as shown in figure 2(*a*). Furthermore, δB_z is negative at the X-point and its neighbouring areas along the neutral sheet. However, in cases B and C, the structure of δB_z along the separatrices becomes more localized and appears to be nearly antisymmetric with respect to the neutral sheet, as shown in figure 2(*b*,*c*), respectively. This localization effect of the quadrupolar structure is sensitive to the

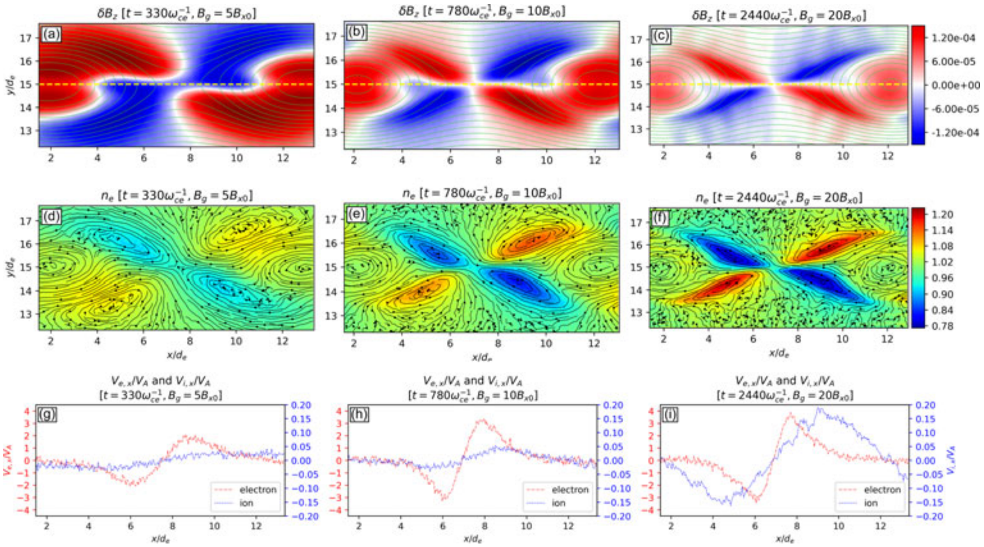

FIGURE 2. (*a,d,g*) Here $t = 330\omega_{ce}^{-1}$ in case A ($B_g = 5B_{x0}$); (*b,e,h*) $t = 780\omega_{ce}^{-1}$ in case B ($B_g = 10B_{x0}$); (*c,f,i*) $t = 2440\omega_{ce}^{-1}$ in case C ($B_g = 20B_{x0}$). (*a–c*) Structure of the out-of-plane magnetic field variations δB_z; (*d–f*) electron density n_e and electron velocity streamlines; (*g–i*) electron velocity $V_{e,x}$ and ion velocity $V_{i,x}$ along x at $y = 15.0$. In each of (*a–c*) and (*d–f*), the three panels share the same colourbar, which is located on the far right-hand side of the row. In (*g–i*), the red line represents the electron velocity $V_{e,x}/V_A$, plotted against the left-hand vertical axis. The blue line represents the ion velocity $V_{i,x}/V_A$, plotted against the right-hand vertical axis. Note that the velocity scales for electrons and ions are different, with $V_{e,x}/V_A$ on the left-hand side and $V_{i,x}/V_A$ on the right-hand side.

guide fields, as it becomes more and more prominent with the increase of the guide field strength, as illustrated in figure 2(*a–c*).

Asymmetric density structures have been observed around the separatrices in standard ion-scale guide field reconnection (Kleva *et al.* 1995; Pritchett & Coroniti 2004; Pritchett 2005; Birn & Priest 2007; Lapenta *et al.* 2011; Markidis *et al.* 2012). It is pointed out that electron parallel motion accelerated by the parallel electric field (along newly reconnected magnetic field lines) contributes to density cavities (low density regions) along one separatrix and density enhancements (high density regions) along the other separatrix. Similar density structures are also obtained in our simulations. Figure 2(*d–f*) illustrate the electron density (represented by the coloured contour plots) in the three simulations. Electron density enhancements develop along the separatrix in the lower left-hand and upper-hand right quadrants. In contrast, electron density cavities reside on the other separatrix in the upper left-hand and lower right-hand quadrants. For clarity, we hereafter refer to them as the 'high-density separatrix' and the 'low-density separatrix', respectively. The in-plane motion of electrons in all cases is shown in figure 2(*d–f*), where streamlines with arrows illustrate the in-plane component of the fluid velocities of electrons. The electron fluid motion exhibits patterns correlated to the out-of-plane magnetic field variations and density asymmetry structures as expected, since these structures are due to the still magnetized electrons carrying the magnetic field in the out-of-plane direction. It is remarked that the spatial extent of both quadrupolar structures and density enhancements/cavities is confined to a few electron inertial lengths in E-REC, typically less than one ion inertial length (d_i) (along the outflow direction). This contrasts with the standard ion-coupled reconnection regime, where such structures generally span several ion inertial lengths (Pritchett & Coroniti 2004). It is noted that the system size in the x direction for all three simulations corresponds to $40\rho_e$, $80\rho_e$ and $160\rho_e$, respectively. These values confirm that the box size is sufficiently large, ensuring that the boundary conditions are not a significant factor in influencing the spatial structure of the reconnection region. As expected, electron and ion velocities also differ in magnitude. Figure 2(*g–i*) illustrate the velocities of electrons and ions (normalized by the Alfvén speed V_A) in the x direction along $y = 15.0$ (marked by the yellow dashed lines in figure 2*a–c*) in all three cases. The electron outflow jets are observed in the results. The ion velocity in the cases A and B is very small as shown in figure 2(*g*,*h*) (the ion velocities are still nearly zero quite far away from the X-point along the current sheet). In standard ion-coupled reconnection, the ion outflow velocity increases linearly from the X-point until reaching the upstream Alfvén speed at the boundary of the ion diffusion region. As a result, the ion flow velocity at the boundary of the electron diffusion region (EDR) (where the electron outflow velocity reaches its peak) should be $(d_e/d_i)V_A = 0.1V_A$ (since the mass ratio is 100 in our simulations), which could be used as a criterion to determine the extent of ion-coupling to the reconnection process. In both case A and case B, the ion velocity $V_{i,x}$ does not reach the $0.1V_A$. The results are consistent with Sharma Pyakurel *et al.* (2019). Furthermore, this also implies that the in-plane currents are predominantly carried by electrons (Kleva *et al.* 1995). In case C, $V_{i,x}$ reaches approximately $0.067V_A$ at the boundary of the EDR. This value is below the commonly cited $0.1V_A$ threshold for ion-coupled reconnection, but it is noticeably higher than in cases A and B, indicating an enhanced ion response.

The guide field has noticeable effects on density structures and particle motion patterns (Kleva *et al.* 1995). With increasing guide field strength, the regions of density enhancement and cavity become narrower, as illustrated in figure 2(*d–f*). Additionally, the maximum (minimum) values in the density enhancement (cavity) regions increase (decrease) with growing guide fields. The δB_z (perturbed magnetic field in the out-of-plane direction), which either adds to or subtracts from the guide field, changes the magnetic pressure. Given the low β, the gas pressure must adjust to approximately balance the total (magnetic plus gas) pressure. Consequently, we obtain $\delta n k_B T \approx \delta(B^2/(2\mu_0)) = B_{z0}\delta B_z/\mu_0$. Therefore, the density variation δn becomes more pronounced when the guide field strength is stronger, as previously discussed in Kleva *et al.* (1995). The narrowing effect also appears in the electron flow results. The in-plane electron velocity exhibits a rotational pattern along local density cavities and enhancement regions. It turns more localized with increasing guide fields, as depicted in figure 2(*d–f*). The difference of δB_z structure is correlated to the density enhancement/cavity region change. The electrons moving along separatrices undergo gyromotion around the magnetic field lines, and their gyroradius becomes smaller as the guide field increases, which leads to the stronger localization of density variation regions. Since the structure of δB_z is caused by the in-plane current, especially the motion of electrons, its structure also narrows with B_g increasing (Pritchett & Coroniti 2004; Swisdak *et al.* 2005). We also observe that the electron velocity increases slightly with larger B_g. We also plot the value of $\sqrt{V_{e,x}^2 + V_{e,y}^2}$ as shown in figure 3, which confirms this result further and exclude the effect of jet rotation (here $V_{e,x}$ and $V_{e,y}$ are the x and y components of electron

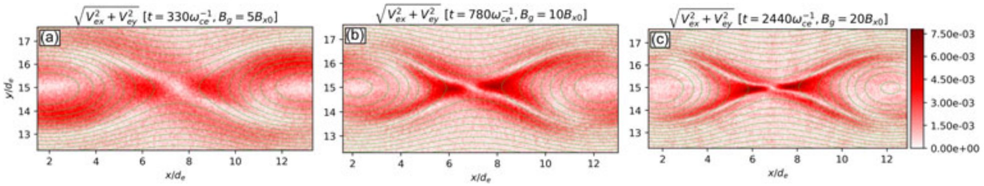

FIGURE 3. The in-plane velocity of electrons in three cases are shown. Here V_{ex} and V_{ey} are the x and y components of electron velocities, respectively.

velocities, respectively). Starting from the electron momentum equation, the Lorentz force term has been identified as contributing to the in-plane electron outflow velocity in E-REC simulations (Guan *et al*. 2024). Consequently, with an increasing guide field, its influence becomes more significant, leading to an enhanced outflow velocity. We find the density variations along the enhancement/cavity regions are relatively modest compared with the background density, a feature notably different from the dramatic variations observed in previous standard ion-coupled reconnection studies (Pritchett & Coroniti 2004; Pritchett 2005). Furthermore, we observe that the density does not show substantial variations inside the islands in the outflow. This is a remarkable difference with respect to ion-coupled reconnection, where density typically increases inside magnetic islands, as reported in Pritchett & Coroniti (2004) and Pritchett (2005). However, our simulation set-up, including the initial equilibrium, boundary conditions, guide field strength and simulation domain, differs significantly from those used in Pritchett's studies. These differences could play a role in the differences we observed, and other in-depth investigations are required to pinpoint the reason for the mismatch.

3.2. *Anisotropic electron heating*

Previous studies on guide field reconnection have revealed anisotropic heating observed at different locations in both experiments and simulations (Guo *et al*. 2017; Pucci *et al*. 2018; Shi *et al*. 2022*a*,*b*, 2023). In this study, we investigate this problem with a broader range of intense guide fields. Figure 4(*a*–*c*) depict the electron temperature anisotropy $A_e = T_{e,\perp}/T_{e,\parallel} - 1$ at the same time as figure 2 for the three simulations, with $T_{e,\perp}$ and $T_{e,\parallel}$ representing the electron temperature perpendicular and parallel to the local magnetic field, respectively. Positive values of A_e indicate that perpendicular temperature exceeds parallel temperature locally (caused by perpendicular heating and/or parallel cooling), whereas negative values of A_e imply that parallel temperature is larger than perpendicular temperature locally (caused by parallel heating and/or perpendicular cooling). Our analysis reveals a consistent presence of significant anisotropy along separatrices in all cases. Specifically, negative anisotropy (depicted by blue regions) is observed along the high-density separatrix and at the X-point, which means that parallel temperature is dominant in these regions. Conversely, positive anisotropy (illustrated by red regions) is situated along the low-density separatrix, indicating relatively larger perpendicular temperature in these areas. However, notable differences are observed with varying guide field strengths. As the guide field increases, the highest value of anisotropy increases, the anisotropic regions narrow, and the zones of positive anisotropy shift closer to the X-point (although A_e remains negative at the X-point). This shift is caused by the reduction of the thickness of the diffusion region. The EDR becomes thinner with the decrease of the electron gyroradius stemming from the larger guide fields (Ricci *et al.* 2004). Since the reconnection rate does not change much, the length of the reconnection region also decreases in the outflow direction. As a result, the positive anisotropy along the separatrix moves closer to the X-point. Apart from the separatrices, pronounced anisotropy also emerges in the outflow regions. In case A (figure 4*a*), negative anisotropy dominates within the outflow regions. Nevertheless, negative anisotropy decreases in magnitude and becomes closer to zero at a certain location (the faint white region near $x \approx 11$, $y \approx 16$ shown in figure 4*b*) in the outflow regions when the guide field increases. In case C, the anisotropy at this location is observed to become positive, as illustrated in figure 4(*c*).

To gain insight into the underlying mechanisms driving the observed temperature anisotropy, we examine the parallel and perpendicular electron temperature (where 'parallel' and 'perpendicular' refer to directions relative to the total local magnetic field, including the guide field), which are defined as $T_{e,\parallel} = \boldsymbol{b} \cdot \boldsymbol{P}_e \cdot \boldsymbol{b}/n_e$ and $T_{e,\perp} = (3\,T_e - T_{e,\parallel})/2$, respectively. Here $\boldsymbol{P}_e$ is the electron pressure tensor, $\boldsymbol{b} = \boldsymbol{B}/|\boldsymbol{B}|$ is the magnetic field unit vector and $T_e = \frac{1}{3} Tr(\boldsymbol{P}_e)/n_e$ is the isotropic electron temperature (with $Tr(\cdot)$ being the trace operator). In figure 4(*d–f*), we show the normalized deviation of electron perpendicular temperature ratio $T_{e,\perp}/T_{e,0} - 1$ ($T_{e,0}$ represents the initial isotropic electron temperature) in all three cases. We find perpendicular temperature increase ($T_{e,\perp}/T_{e,0} - 1 > 0$) along the low-density separatrix. In contrast, perpendicular temperature decrease ($T_{e\perp}/T_{e,0} - 1 < 0$) is observed along the high-density separatrix. Additionally, we observe that the regions of perpendicular temperature increase and decrease narrow as the guide field strength increases.

Recent experimental studies found that E-REC with strong guide fields is accompanied by parallel heating along one separatrix (Shi *et al.* 2023), which is attributed to the parallel electric field. Here we show the normalized deviation of electron parallel temperature ratio $T_{e,\parallel}/T_{e,0} - 1$ from our three simulations in figure 4(*g–i*). Our results reveal parallel temperature increases along the high-density separatrix, consistent with experiments (Shi *et al.* 2023). However, we also observe parallel temperature decreases along the low-density separatrix. Furthermore, the parallel temperature increase and decrease are significantly influenced by the magnitude of the guide field. With increasing guide field strength, the parallel temperature increase/decrease regions become thinner and more localized, and the magnitude of the parallel temperature increase/decrease changes notably. It is also evident from the colourbar in figures 4(*c–f*) and 4(*g–i*) that the variations in the parallel temperature ratio $T_{e,\parallel}/T_{e,0}$ exceed those in the perpendicular temperature ratio $T_{e,\perp}/T_{e,0}$, particularly in case C where the guide field is stronger. As a consequence, the parallel temperature ratio $T_{e,\parallel}/T_{e,0}$ shows more correlation with the spatial distribution of A_e than perpendicular temperature ratio $T_{e,\perp}/T_{e,0}$. Both the spatial distribution of $T_{e,\parallel}/T_{e,0}$ and A_e illustrate a transition from a quadrupolar to a hexapolar to an octopolar structure as the guide field increases. Specifically speaking, in simulation A, A_e shows a quadrupolar pattern, with two positive bands located on the low-density separatrix and the other two negative bands along the other separatrix and within the outflow regions. In simulation B, A_e exhibits a hexapolar structure. In addition to the quadrupolar structure similar to that observed in figure 4(*a*), there is a faint band (where A_e is almost zero near $x \approx 11$, $y \approx 16$ downstream of the separatrix, which is absent in simulation A. These two faint bands (there is also a faint band in the left-half of the domain) segregate the negative bands along the separatrix from those within the outflow regions, culminating in a pronounced hexapolar

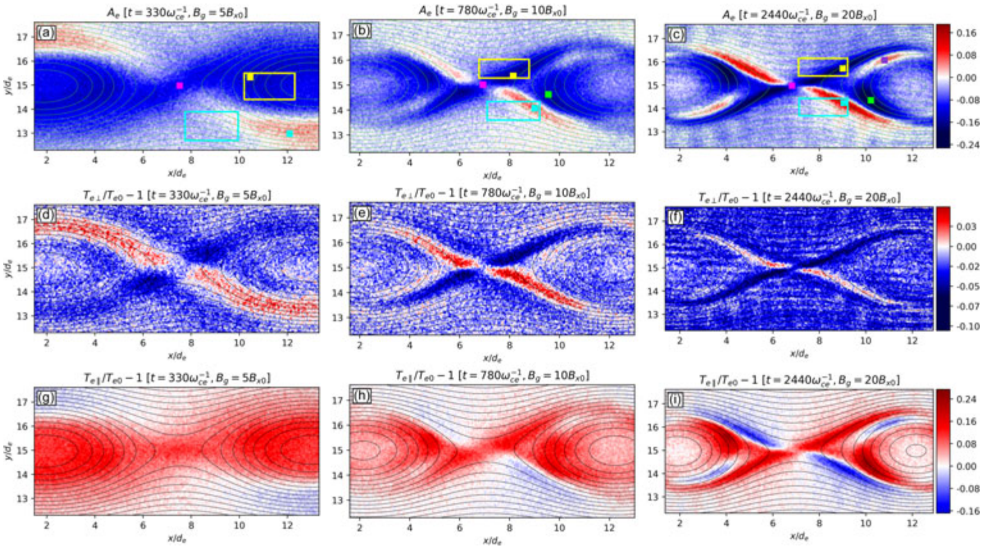

FIGURE 4. Electron temperature anisotropy A_e, normalized deviation of perpendicular and parallel temperatures: $T_{e,\perp}/T_{e,0} - 1$ and $T_{e,\parallel}/T_{e,0} - 1$ in the three cases. Here $T_{e,0}$ is the initial electron temperature. The coloured boxes represent the positions at which EVDFs are calculated in these three cases. The rectangle regions in (*a–c*) represent the areas selected for plotting scatter plots of $T_{e,\parallel}$ and $(n/B)^2$ which are shown in details below. In each row, the three panels share the same colourbar, which is located on the far right-hand side of the row.

structure in both A_e and $T_{e,\parallel}$. In simulation C, an octopolar structure appears, which features two positive bands on one separatrix paired with two negative bands along the other separatrix. Additionally, there are two bipolar alternations of positive and negative temperature anisotropy bands inside the outflow regions and downstream of the separatrix, which is a unique characteristic in this case. Essentially, our analysis shows that E-REC produces different electron temperature anisotropy patterns under varied guide fields, with more parallel temperature increase/decrease features developing in magnetic islands as the guide field strength increases.

In order to exclude the possibility of the results being influenced by plasma recirculation, We have calculated the recirculation times for two conditions of the guide field, $B_g = 10B_{x0}$ and $B_g = 20B_{x0}$ (since the new features appear in these two cases).

(i) For $B_g = 10B_{x0}$, where the box size $L = 2d_i$ and the maximum electron outflow velocity in the x direction $V_{ex,\max} = 0.006c$ (c is the speed of light), the recirculation time Δt is computed as

$$\Delta t = \frac{L}{V_{ex,\max}} \approx 333\omega_{pi}^{-1} = 666\omega_{ce}^{-1}. \tag{3.1}$$

Given that the reconnection evolution time from figure 1(*b*) is approximately $530\omega_{ce}^{-1}$ (starting from when the reconnection rate is above zero (which is $\approx 250\omega_{ce}^{-1}$) and ending at the time when we do analyses), it is evident that the observed structures are not a result of recirculation.

(ii) For $B_g = 20B_{x0}$, with $V_{ex,\max} = 0.007c$, the calculated recirculation time is

$$\Delta t \approx 286\omega_{pi}^{-1} = 1143\omega_{ce}^{-1}. \tag{3.2}$$

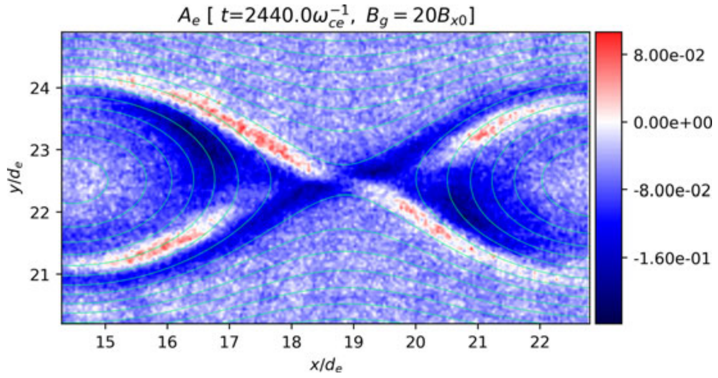

FIGURE 5. In case D, with a significantly larger simulation box ($L_x = 6d_i$, $L_y = 3d_i$), the electron anisotropy results align with those shown at the same time snapshot as figure 4(*c*). Similar patterns of anisotropy are observed, with positive A_e (red regions) appearing along one separatrix and within the outflow regions.

> Considering the evolution time of $1740\omega_{ce}^{-1}$ from figure 1(*c*) (starting from when the reconnection rate is above zero (which is $\approx 700\omega_{ce}^{-1}$) and ending at the time when we do analyses), and recognizing that the actual velocity is much lower than the maximum value used here, the real recirculation time would be considerably longer.

To provide more compelling evidence, we have conducted an additional simulation using a larger simulation box, specifically $L_x = 6d_i$, $L_y = 3d_i$ (case D), with a guide field of $B_g = 20B_{x0}$. This simulation yielded similar anisotropy results. In this case, the analysis was undertaken at a time corresponding to that depicted in figure 4(*c*). The electron temperature anisotropy results for case D are shown in figure 5. We also calculated the recirculation time for case D. We found the electron outflow jet velocities are comparable to that of case C. Since the box side lengths are three times larger, the corresponding recirculation times are also proportionally longer: $\Delta t \approx 3429\omega_{ce}^{-1}$ for case D. This indicates that the recirculation time in this larger simulation box is significantly greater than the time at which positive anisotropy in the exhaust is observed (i.e. $1740\omega_{ce}^{-1}$ as mentioned above). Notably, the recirculation time also exceeds the total analysis time (the time we do analyses, i.e. $t = 2440\omega_{ce}^{-1}$), providing robust evidence supporting our argument. It should be noted that the choice of vertical length $L_y = 3d_i$ in case D does not result in interactions between the two current sheets, as the reconnection along the lower sheet remains in an early phase and no interactions are observed at the time of analysis. Furthermore, the reconnection in case D remains within the electron-only regime. Consequently, we affirm the results are not caused by recirculation.

3.3. *Electron velocity distribution functions*

In the previous section, we analysed the electron temperature anisotropy observed in the three cases, highlighting the notable variations that take place as the guide field strength increases. In this section, we further examine the EVDFs at different spatial locations. First, we analyse the EVDFs at the X-point in the three cases. We also focus on regions exhibiting pronounced anisotropy, where we observe a transition from a quadrupolar to a hexapolar to an octopolar structure as the guide field intensity increases. Figure 4 illustrates the selected positions where EVDFs are calculated, denoted by coloured square boxes whose side is approximately $0.3d_e$, each containing approximately 500 000 electron macroparticles. We only sample macroparticles within the bands in the right-half of the domain since the structure of the reconnection region is symmetrical, and we find analogous results in the left-half of the domain (not shown here).

Figure 6 presents the 2-D projections of the EVDFs at different locations in case A. Each row has four panels, with the initial three depicting the normalized microscopic electron velocity components centred to their mean values, i.e. $w_{\parallel}/v_{th,e} = (v_{\parallel} - v_{\parallel,\mathrm{mean}})/v_{th,e}$, $w_{\perp 1}/v_{th,e} = (v_{\perp 1} - v_{\perp 1,\mathrm{mean}})/v_{th,e}$ and $w_{\perp 2}/v_{th,e} = (v_{\perp 2} - v_{\perp 2,\mathrm{mean}})/v_{th,e}$, respectively. The last panel in each row represents the one-dimensional (1-D) histogram of these three components with 256 bins. The velocity components are defined as follows (the same as Goldman, Newman & Lapenta (2016) and Arrò *et al.* (2023)): $v_{\parallel}$ aligns with the local magnetic field $\boldsymbol{B}$, $v_{\perp 1}$ points towards $\boldsymbol{B} \times \hat{z}$ and $v_{\perp 2}$ is oriented in the direction of $\boldsymbol{B} \times \boldsymbol{v}_{\perp 1}$. Here $v_{\parallel,\mathrm{mean}}$, $v_{\perp 1,\mathrm{mean}}$ and $v_{\perp 2,\mathrm{mean}}$ denote the fluid drift velocity in each direction and have been subtracted. Here $v_{th,e}$ represents the initial electron thermal velocity. The colourbar of 2-D plots and the y axis of the 1-D histogram indicate the number of macroparticles.

Figure 6(*a–d*) corresponds to the magenta box (X-point). Figures 6(*a*) and 6(*b*) indicate evident skewness in $v_{\parallel}$, implying a net parallel heat flux density. This observation is supported by figure 6(*d*). We also find the agyrotropy is very small from figure 6(*c*) where the projection of the EVDFs on the $v_{\perp 1} - v_{\perp 2}$ plane is almost rotationally symmetric. Agyrotropy represents the asymmetry in the velocity distribution of particles within the plane perpendicular to the magnetic field. It is used to measure the degree to which the velocity distribution deviates from gyrotropy. The near rotational symmetry indicates that the EVDFs are close to gyrotropic in our simulations, though small finite agyrotropy also exists. Additionally, in figure 4(*g*), parallel heating is evident in this region, corroborated by the slightly irregular oval-shaped EVDFs in figure 6(*a*,*b*). Figure 6(*e–h*) depicts the EVDFs of the yellow box (outflow region). Figure 6(*e*,*f*) also display irregular oval-shaped EVDFs, consistent with the parallel heating observed in the outflow region in figure 4(*g*). Skewness is also apparent in figure 6(*h*), while figure 6(*g*) illustrates small agyrotropy in this region. Similar agyrotropic characteristics are observed in the cyan box (the separatrix in the lower right-hand quadrant), as depicted in figure 6(*k*). This region contrasts with the former two, exhibiting perpendicular heating and parallel cooling, as evidenced in figure 4(*d*,*g*). As a consequence, the EVDFs in figure 6(*i*,*j*) exhibit slightly irregular vertical oval shapes. Figure 6(*l*) indicates that the perpendicular heating is relatively small in this region since the broadening of the perpendicular velocities is not very pronounced with respect to the parallel component.

Figure 7 illustrates the 2-D projections of the EVDFs at four locations in case B. The first row corresponds to the magenta box (X-point), where the skewness similar to case A is observed in figures 7(*a*) and 7(*b*). The skewness is also evident in the 1-D histogram (figure 7*d*). Figure 7(*c*) displays a distribution that is predominantly gyrotropic, with small but finite agyrotropy, which is also observed for EVDFs calculated inside the other three boxes (figures 7*g*, 7*k* and 7*o*) in case B. Figure 7(*e–h*) shows the EVDFs of the yellow box. Due to the parallel heating in this area, the velocity distribution becomes broader in the parallel direction. Consequently, figures 7(*e*) and 7(*f*) display oval-shaped distributions, which are more pronounced than those observed in the yellow box of case A. The parallel heating is also highlighted in figure 7(*h*). On the other hand, the cyan box experiences parallel cooling

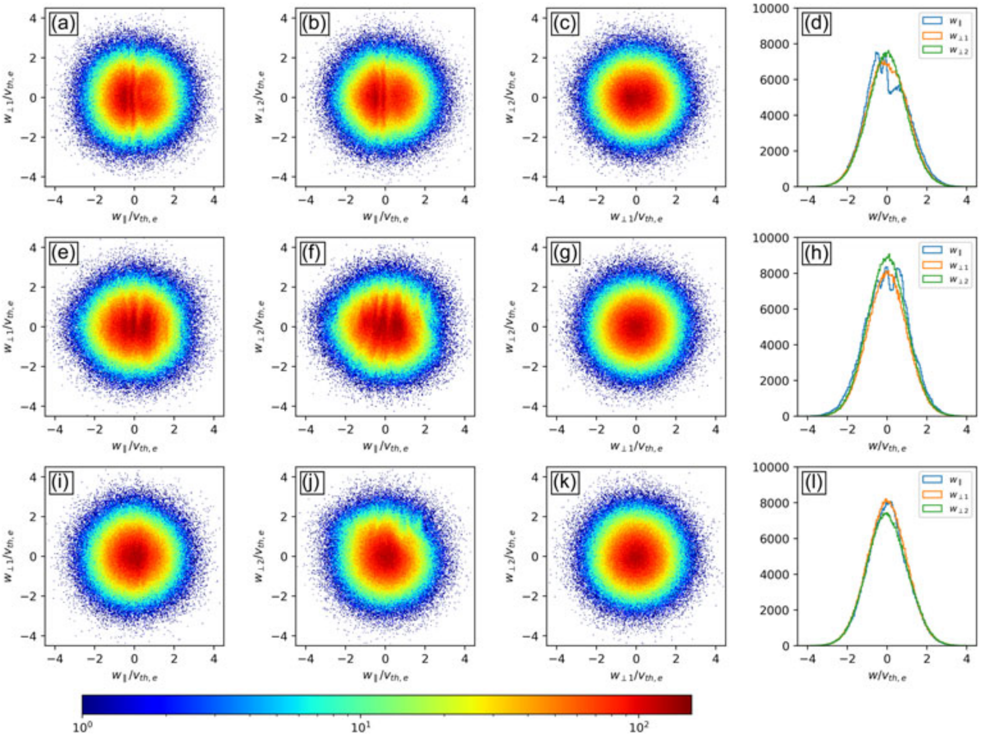

FIGURE 6. The EVDFs in case A are depicted as follows: (*a–d*) correspond to the magenta box (the X-point with negative A_e); (*e–h*) correspond to the yellow box (the outflow region with negative A_e); and (*i–l*) correspond to the cyan box (the separatrix in the lower right quadrant with positive A_e). The colourbar indicates the particle count. Panels (*a,e,i*), (*b,f,j*) and (*c,g,k*) display the projections of EVDFs in distinct planes, while (*d,h,l*) illustrate the 1-D EVDFs, with the *y* axis denoting the number of particles.

and perpendicular heating. Therefore, the EVDFs appear elongated in the directions perpendicular to the local magnetic field, as demonstrated in figures 7(*i*) and 7(*j*). Figure 7(*l*) displays the perpendicular heating more distinctly as the two perpendicular components become wider. Figure 7(*m–p*) demonstrates the EVDFs of the lime box, which also presents prominent parallel heating. Correspondingly, figures 7(*m*) and 7(*n*) show that 2-D EVDFs are elongated in the parallel direction. However, their shapes are irregular, as also shown in figure 7(*p*), which is significantly different from the yellow box in case A (also located in the outflow region).

In figure 8, we show the 2-D projections of the EVDFs at five locations in case C. Figure 8(*a–d*) illustrate the EVDFs of the magenta box (X-point). Figures 8(*a*) and 8(*b*) suggest a skewed parallel velocity component, similar to the magenta boxes in cases A and B. Figure 8(*d*) represents the 1-D EVDFs that confirm this skewness, indicating a significant heat flux density near the X-point in case C. Figure 8(*c*) reveals that the EVDFs in the magenta box are close to gyrotropic, a feature that becomes more notable as the guide field increases as the core region becomes more rotationally symmetric in figure 8(*c*) compared with figures 6(*c*) and 7(*c*). In fact, the EVDFs of all five boxes show predominantly gyrotropic features in case C, as shown in figures 8(*g*), 8(*k*), 8(*o*) and 8(*s*). Remarkable anisotropy and parallel heating along the separatrix in the upper right-hand quadrant (the yellow box) is

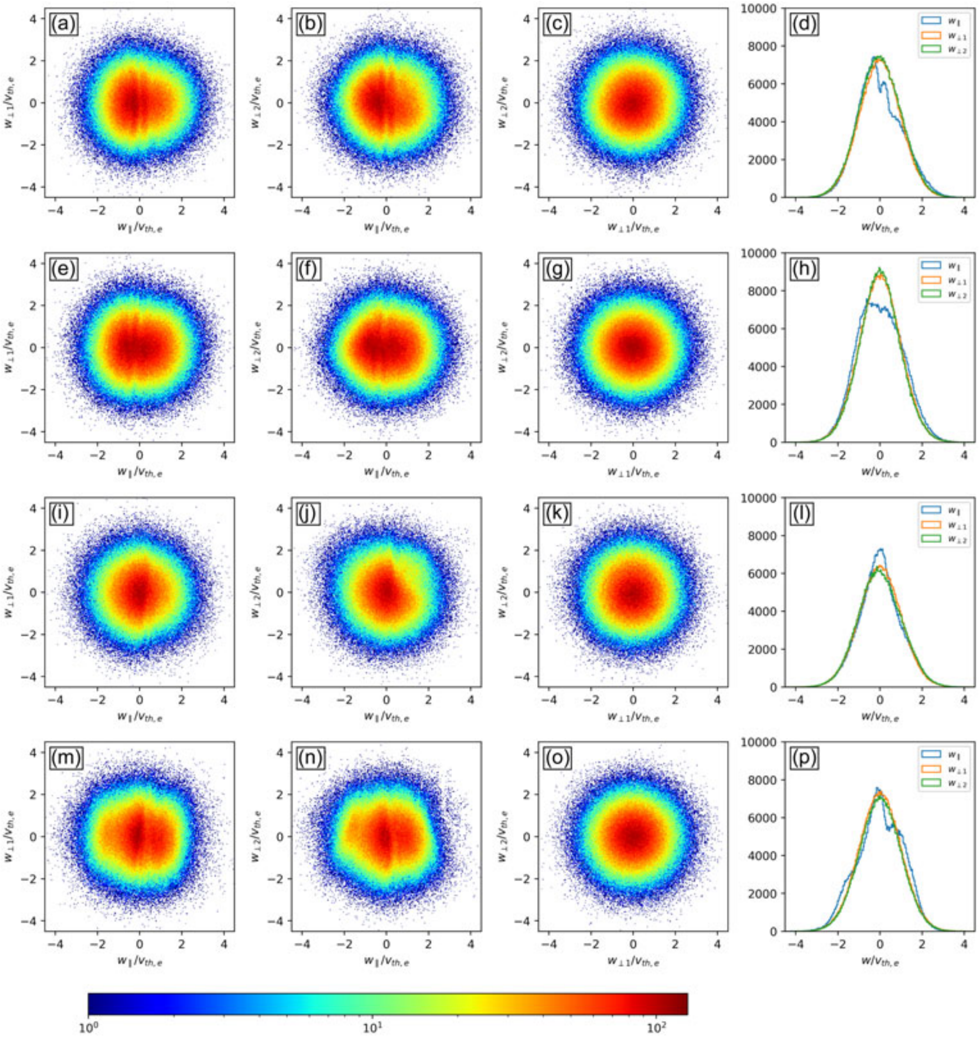

FIGURE 7. The EVDFs in case B are depicted as follows: (*a–d*) correspond to the magenta box (the X-point with negative A_e); (*e–h*) correspond to the yellow box (the separatrix in the upper right-hand quadrant with negative A_e); (*i–l*) correspond to the cyan box (the separatrix in the lower right-hand quadrant with positive A_e); and (*m–p*) correspond to the lime box (the outflow region with negative A_e). The colourbar indicates the particle count. Panels (*a,e,i,m*), (*b,f,j,n*) and (*c,g,k,o*) display the projections of EVDFs in different planes, while the (*d,h,l,p*) represent the 1-D EVDFs, with the *y* axis denoting the number of particles.

observed in figure 4(*c*,*i*). Figure 8(*e*–*h*) shows the EVDFs of the yellow box. Due to the parallel heating, oval-shaped non-Maxwellian EVDFs appear, as shown in figures 8(*e*) and 8(*f*). Figure 8(*h*) also clearly displays that the parallel velocity component becomes wider. It is also noted that the oval-shaped EVDFs become more regular and elongated in case C, compared with cases A and B. Correspondingly, the $T_{e,\parallel}$ of the yellow box in case C also becomes larger than in the other two cases, as shown in figure 4(*g*–*i*). Figure 8(*i*–*l*) depicts the EVDFs of the cyan box. Both parallel cooling and perpendicular heating exist along this separatrix in the lower right-hand quadrant, leading to the formation of vertically elongated EVDFs, as illustrated in figures 8(*i*) and 8(*j*). The parallel cooling is illustrated more clearly in the 1-D histograms as $w_\parallel/v_{th,e}$ becomes narrower (figure 8*l*). The EVDFs in the cyan box, which are close to gyrotropic and exhibit small finite agyrotropy, suggest that the heating is close to isotropic within the plane perpendicular to the local magnetic field. Figure 8(*m–p*) illustrates the EVDFs of the lime box. Figures 8(*m*) and 8(*n*) show EVDFs that are stretched along the parallel direction, corresponding to the parallel heating observed in this region in figure 4(*i*). In addition, the skewness in figure 8(*p*) denotes relatively large heat flux density in this area. However, the EVDFs projected in the parallel direction become irregular. Figure 8(*q–t*) demonstrates the EVDFs of the purple box, which exhibit different features from the other boxes. A flat-top parallel velocity distribution is observed for particles with small random velocity (the velocity of particles relative to the bulk velocity) in the parallel direction, while parallel cooling emerges for particles with large random velocity in the parallel direction, as shown in figures 8(*q*), 8(*r*) and 8(*t*), where 2-D EVDFs appear stretched in perpendicular directions and compressed in the parallel direction.

To explore the causes of the temperature anisotropy and the EVDFs observed along separatrices, we analyse the relationship among electron density n, magnetic field strength B and electron parallel temperature $T_{e\parallel}$. According to the CGL theory, the following scaling relation holds (Bittencourt 2013):

$$\frac{T_{e\parallel}B^2}{n^2} = \text{constant}. \tag{3.3}$$

We plot $T_{e\parallel}$ against n^2/B^2 for each of the three cases to examine their alignment with CGL theory prediction or the Boltzmann condition (Chew, Goldberger & Low 1956; Snyder *et al.* 1997; Wetherton *et al.* 2019). From the CGL relation, we can derive

$$T_{e\parallel} \propto \left(\frac{n^2}{B^2}\right), \tag{3.4}$$

which means $T_{e\parallel}$ and n^2/B^2 have a positive linear relationship. In comparison, the Boltzmann response is a horizontal line, as $T_{e\parallel}$ remains constant regardless of n and B. The scatter plots of $T_{e\parallel}$ versus n^2/B^2 provide insight into whether the simulations adhere to the CGL predictions (Wetherton *et al.* 2021; Oka *et al.* 2023).

For each of the three simulations with varying guide field strengths, we select data points residing on the separatrix regions, which encompass both high-density and low-density areas. In order to also show their relationship under moderate density, we also cover the regions neighbouring to the separatrices. The regions we selected are shown in figure 4(*a–c*), represented by the cyan and yellow rectangles. From these regions, we extract values of electron density n, magnetic field strength B and electron parallel temperature $T_{e\parallel}$. We then create scatter plots of $T_{e\parallel}$ versus n^2/B^2 for each simulation as shown in figure 9 (the three quantities ($T_{e\parallel}$, n and B) are all normalized by their respective mean values).

(i) Case A – ($B_g = 5B_{x0}$). At lower values of n^2/B^2 (corresponding to the low-density regions since the variations of B^2 are very slight in the domain), $T_{e\parallel}$ remains approximately constant, indicating Boltzmann-like behaviour. As n^2/B^2 increases, $T_{e\parallel}$ also increases modestly, indicating the onset of CGL effects. This suggests that the system predominantly exhibits Boltzmann-like

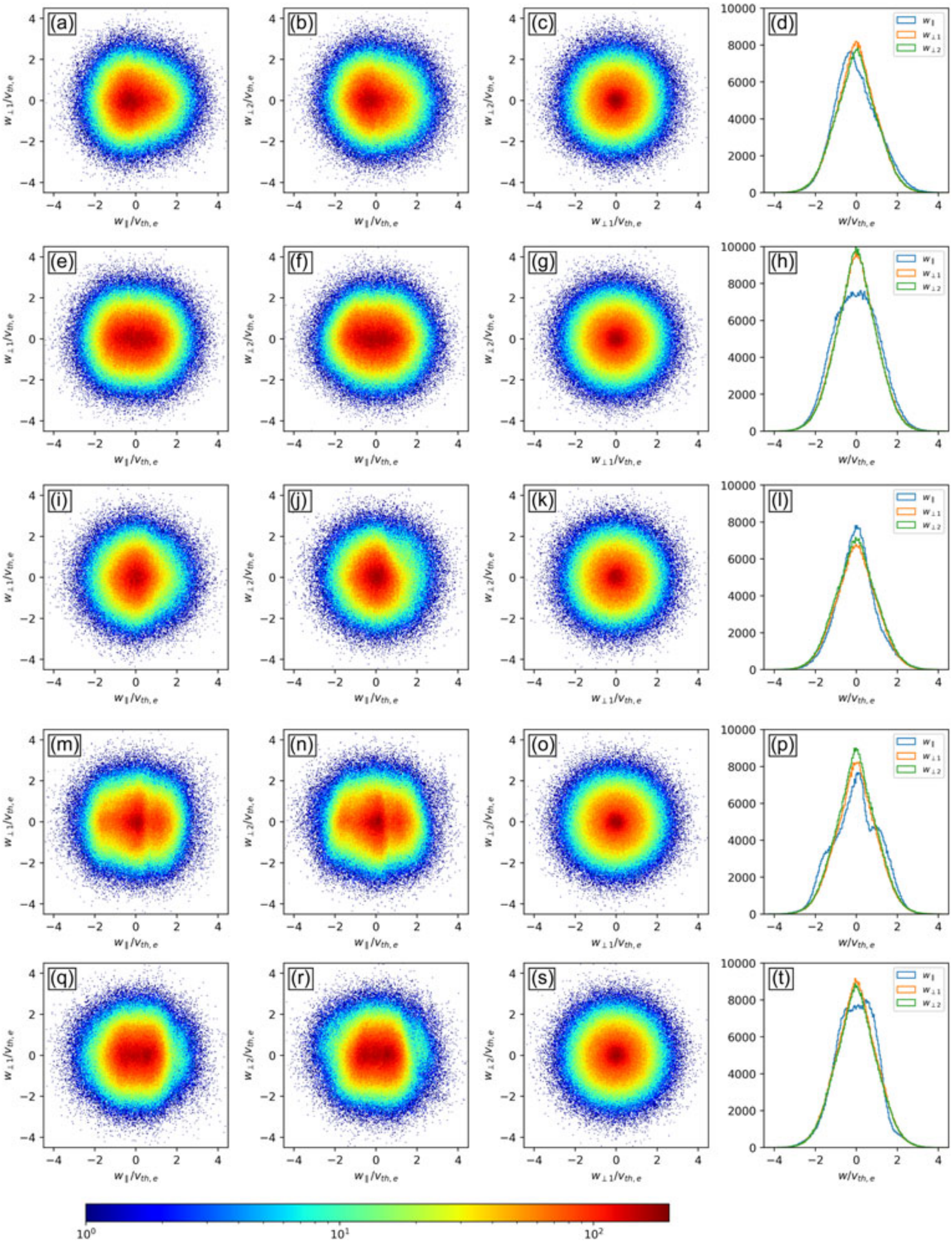

FIGURE 8. The EVDFs in case C: (*a–d*) correspond to the magenta box (the X-point with negative A_e); (*e–h*) correspond to the yellow box (the separatrix in the upper right-hand quadrant with negative A_e); (*i–l*) correspond to the cyan box (the separatrix in the lower right-hand quadrant with positive A_e); (*m–p*) correspond to the lime box (the outflow region with negative A_e); (*q–t*) correspond to the purple box (the outflow region with positive A_e). The colourbar indicates the particle count. Panels (*a,e,i,m,q*), (*b,f,j,n,r*) and (*c,g,k,o,s*) are the projections of EVDFs in different planes. Panels (*d,h,l,p,t*) represent the 1-D EVDFs, with the *y* axis denoting the number of particles.

behaviour at lower n^2/B^2 values, where electron heat conduction effectively maintains temperature isotropy. The slight increase in $T_{e\|}$ at higher n^2/B^2 indicates the onset of CGL relation, showing that adiabatic effects start to influence the electron temperature.

(ii) Case B – ($B_g = 10B_{x0}$). The relationship shows a more pronounced increase in $T_{e\|}$ with n^2/B^2, exhibiting a transitional behaviour between Boltzmann and CGL effects. This indicates that the system is in an intermediate regime where both heat conduction and adiabatic effects significantly influence the electron temperature. The increased guide field strength enhances the influence of adiabatic processes, resulting in more noticeable CGL characteristics.

(iii) Case C – ($B_g = 20B_{x0}$). The scatter plot shows an almost linear relationship between $T_{e\|}$ and n^2/B^2, suggesting a strong alignment with CGL theory and adiabatic processes dominating the electron temperature.

However, the presence of finite parallel heat flux in all simulations (as shown in figure 11) may be considered deviations from the ideal CGL behaviour, where zero heat flux is assumed. We note, nevertheless, that within the CGL model the heat flux is assumed to be zero as part of the mathematical closure of the fluid moment hierarchy. As a result, the heat flux density is not necessarily zero in fully kinetic simulations of a system approaching ideal CGL behaviour (see discussion in Allmann-Rahn, Trost & Grauer (2018)). In this context, we do not interpret the presence of non-zero heat flux density in our simulations as a contradiction to CGL-like behaviour, and we consider that our three cases lie in a transitional regime where both thermal conduction and adiabatic effects coexist. It is also noted that the parallel heat flux intensity increases as the guide field strength enhances, which might be caused by the presence of multiple populations (Hwang *et al.* 2019; Lavraud *et al.* 2021) and warrants further investigation. These findings provide an explanation for the electron parallel temperature variations observed along the separatrices. Since the parallel velocity component in the EVDFs must be consistent with the parallel temperature variations, they also elucidate the causes of the EVDFs' shape along the separatrices we observed in all three cases.

The electric field causes a skewed velocity distribution function along its direction by accelerating or decelerating particles (Whealton & Woo 1972). In our simulations, the parallel electric field mainly resides near the X-point (here 'parallel' means the direction parallel to the local magnetic field), which accelerates electrons in the negative direction and causes the negative-skewed EVDFs features at the X-point in all three cases (here 'negative-skewed' means the parallel velocity components of the EVDFs at the X-point is skewed towards the negative direction, as shown in figures 6*d*, 7*d* and 8*d*).

It is also noted that the selected yellow box for run A in figure 4(*a*) is not exactly adjacent to the separatrix, unlike those in runs B and C. This is because in run A, the region near the separatrix exhibited very limited variation in local density, while showing a significant density difference between the two boxes. As shown in figure 2(*d*), the density enhancement and cavity regions in run A occupy a relatively larger area compared with runs B and C. If we had chosen a box very close to the separatrix, the individual boxes would contain nearly uniform density values, and the span of $(n/B)^2$ would be narrow. Consequently, the resulting comparison between $T_{e\|}$ and $(n/B)^2$ would not sufficiently reveal the scaling trend expected from the CGL relation. To ensure a meaningful spread in $(n/B)^2$, which is crucial for visualizing

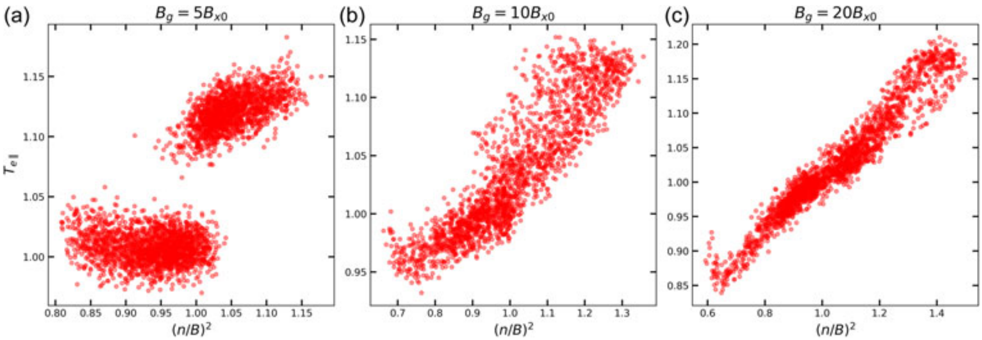

FIGURE 9. Scatter plot of the relationship between electron parallel temperature $T_{e\parallel}$ and $(n/B)^2$ in three cases, where n is electron number density and B is magnetic field strength. The three quantities ($T_{e\parallel}$, n and B) are all normalized by their mean value.

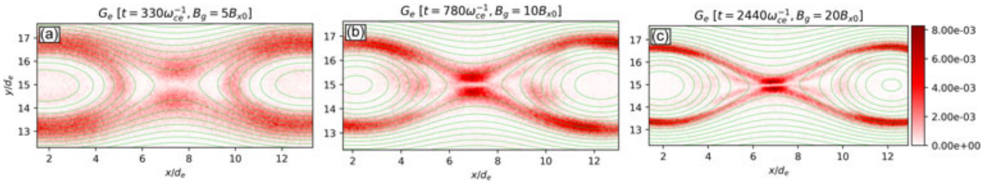

FIGURE 10. Electron agyrotropy G_e in all three cases. The three panels share the same colourbar, which is located on the far right-hand side of the figure.

the CGL-like trend, we deliberately selected the current box placement. As a result, the deviation from CGL predictions in run A, as shown in figure 9(a), might be related to the box location. Nevertheless, we would like to emphasize that even in run A, a linear trend between $T_{e\parallel}$ and $(n/B)^2$ is still visible in the high-density portion (i.e. large $(n/B)^2$ values) of figure 9(a), indicating that CGL-like behaviour is still present to some extent.

In summary, by investigating the EVDFs in our three runs, we find that with the increase of guide field strength and the resultant reduction of electron gyroradius, the electron parallel velocity component changes remarkably (especially the electrons in the outflow regions). Different types of EVDFs are observed as the guide field strength increases, and the most various features are obtained in the case of the strongest guide field studied in this work. Notably, the EVDFs of all the examined locations in the three cases are close to gyrotropic. Figure 10 illustrates the agyrotropy in three cases (calculated using the formula in Swisdak (2016)) and its magnitude is very small. This indicates that the EVDFs are close to gyrotropic in such intense guide field conditions, while the agyrotropy could be large when the guide field is relatively low (Gao *et al.* 2023).

Figure 11 illustrates the electron heat flux density in the parallel direction, normalized to the reference electron heat flux density $q_0 = n_0 m_e v_{th,e}^3$ (where n_0 is the initial density), for all three runs. These plots show the presence of finite positive parallel electron heat flux density at the X-point, extending to the separatrices as the guide field increases, which is consistent with the EVDFs observed above. Intense heat flux density is also evident in the outflow regions, albeit with a direction opposite to that

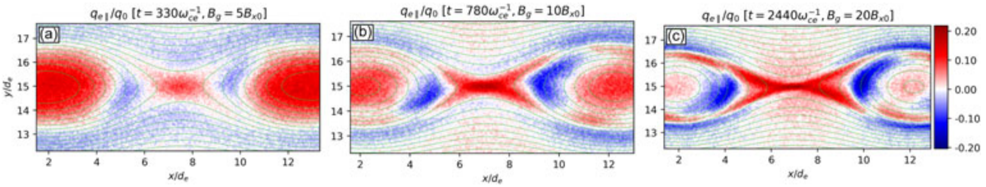

FIGURE 11. Electron heat flux density in the parallel direction (with respect to the local magnetic field) in all three cases, normalized to the reference electron heat flux density $q_0 = n_0\, m_e\, v_{th,e}^3$. The three figures share the same colourbar, which is located on the far right-hand side of the figure.

observed in the aforementioned regions. As the guide field intensifies, the region exhibiting intense heat flux density becomes narrower, and the magnitude of the normalized heat flux density along the separatrices and within the outflow regions increases. Positive heat flux density is also present at the centre of the magnetic islands, but its amplitude decreases with increasing guide field strength.

4. Discussion and conclusions

Electron-only reconnection with various strengths of guide fields is systematically investigated by means of 2-D fully kinetic PIC simulations, focusing on anisotropic heating and EVDFs. The guide field delays the onset of E-REC, similar to what has been observed in previous studies regarding standard ion-scale reconnection (Pritchett 2005; Birn & Priest 2007). The in-plane electron current leads to out-of-plane magnetic field variations, consistent with the Hall quadrupolar configuration (Birn & Priest 2007). Asymmetric quadrupolar electron density structures are also observed, with density enhancements on one separatrix and density cavities along the other (Muñoz & Büchner 2016). It is noted that the ion outflow jets are significantly smaller than the upstream Alfvén speed in our simulations, which is consistent with features typically observed in E-REC (Phan *et al.* 2018). However, we also note that the ion response in case C is stronger than in cases A and B, suggesting a greater degree of ion involvement. Stronger guide fields narrow the density enhancements/cavities and the out-of-plane magnetic field quadrupolar structures (Kleva *et al.* 1995; Birn & Priest 2007). This narrowing effect might be related to non-ideal kinetic effects which take place at scales of the order of the electron gyroradius, producing electron-scale fluctuations and structures where electrons eventually decouple from the magnetic field dynamics. As the guide field intensifies, it is reasonable to think that the non-ideal regions will become thinner since their size is of the order of the electron gyroradius and stronger guide fields imply smaller gyroradii. We plan to investigate this problem in future work.

Temperature anisotropy is observed along separatrices and inside magnetic islands. The analysis of $T_{e,\perp}$ demonstrates that perpendicular temperature increase resides along the low-density separatrix, and perpendicular temperature decrease is present on the other separatrix. Parallel temperature increase, on the other hand, appears on the separatrix displaying perpendicular temperature decrease. It is also noted that parallel temperature decrease manifests on the separatrix showing perpendicular temperature increase. However, the parallel temperature increase/decrease is stronger than the perpendicular temperature increase/decrease in our simulations. The guide field intensity has notable effects on the spatial distribution of the parallel electron temperature (Pucci *et al.* 2018). As the guide field increases, both the regions of parallel and perpendicular temperature increase/decrease become narrower, and parallel temperature increase/decrease exhibits different structures inside magnetic islands, which generates different non-Maxwellian EVDFs in outflow regions (Muñoz & Büchner 2016; Shi *et al.* 2022*a*). Furthermore, we observe a transition from a quadrupolar to a hexapolar to an octopolar structure in the parallel electron temperature and the temperature anisotropy as the guide field intensity increases.

The EVDFs across different locations are examined in all three cases. The perpendicular velocity components of these three cases exhibit a close-to-gyrotropic distribution, although small finite agyrotropy is observed. The EVDFs near the X-point show velocity distributions with skewness in the direction of the local magnetic field, indicating the existence of relatively large heat flux density. The observed EVDF shapes are consistent with the underlying anisotropic temperature distributions. At the separatrices exhibiting parallel heating and perpendicular cooling, the EVDFs are elongated along the magnetic field direction. In contrast, where perpendicular heating dominates, the EVDFs stretch in the plane perpendicular to the magnetic field. The guide field is found to have notable effects on the parallel velocity component, especially on electrons in the outflow regions. The shapes of the EVDFs are sensitive to the guide field strength and various features develop as the guide field intensifies. Finite electron heat flux density in the parallel direction is observed at the X-point, along the separatrices and inside magnetic islands. Our analyses show that the three simulations ($B_g/B_{x0} = 5$, 10, and 20) exhibit features of the CGL theory. As the guide field increases, the system is more consistent with the CGL theory predictions. However, the parallel heat flux exists in our simulations, which might be partly related to the presence of multiple populations. We note that the presence of parallel heat flux density is not unexpected in fully kinetic systems that lie in a transitional regime exhibiting intermediate features between thermal conduction and adiabatic behaviour. This provides an explanation for the electron parallel temperature variations observed along the separatrices, as well as for the causes of the EVDFs' shape along separatrices in all three cases.

The pressure anisotropy observed in our simulations under increasing guide field strength exhibits features similar to those associated with Regime 4 in Le *et al.* (2013). A detailed quantitative comparison across different parameter ranges will be explored in future studies. Next, we plan to focus on analysing case C ($B_g = 20B_{x0}$) in follow-up work. We aim to explore theoretical models that incorporate finite heat flux effects to better understand these deviations from ideal CGL behaviour. This work might provide insights into the understanding of electron heating and heat flux density in the E-REC observed in the turbulent magnetosheath (Phan *et al.* 2018).

The parallel temperature increase observed along one separatrix in our simulations is consistent with a recent experimental study (Shi *et al.* 2023). However, a discrepancy arises regarding perpendicular temperature increase: while it only emerges along the low-density separatrix in our simulations, perpendicular heating is observed on both separatrices in experiments. This inconsistency may stem from 3-D and/or collisional effects as pointed out in Shi *et al.* (2023) and we plan to pursue further investigations in future studies. Besides, we also plan to investigate the influence of different initial equilibrium configurations (like Harris current sheets) and different boundary conditions (like open boundary conditions) on the reconnection process. Since there is a large out-of-plane magnetic field in the centre of the current sheet in the force-free equilibrium and it might affect the evolution of reconnection structure, using other equilibria would assist us in understanding the potential impact of initial conditions on the simulation results, such as the out-of-plane magnetic field structure, density variations, etc. In addition, we also observed the thin alignment features along the parallel direction in the EVDFs and their broadening trend with increasing guide field. This might be related to specific dynamic processes and we plan to investigate them in future work as well.

Acknowledgements

J.R. gratefully acknowledges Professor J. Egedal for insightful discussions on the simulation results. We gratefully acknowledge the Gauss Centre for Supercomputing e.V. (www.gauss-centre.eu) for providing computing time on the GCS Supercomputer SuperMUC-NG at Leibniz Supercomputing Centre (www.lrz.de) through the project 'Heat flux regulation by collisionless processes in heliospheric plasmas - ARIEL' and 'Investigation of suprathermal features in the velocity distribution functions of space and astrophysical plasmas-SupraSpace'. The resources and services used in this work were also provided by the VSC (Flemish Supercomputer Center), funded by the Research Foundation – Flanders (FWO) and the Flemish Government.

Editor Francesco Califano thanks the referees for their advice in evaluating this article.

Funding

This project has received funding from the KU Leuven Bijzonder Onderzoeksfonds (BOF) under the C1 project TRACESpace, and from the FWO project Helioskill (G0B9923N). J.R. is partially supported by the CSC (China Scholarship Council)-IMEC-KU Leuven Scholarship Programme. M.E.I. acknowledges support from the Deutsche Forschungsgemeinschaft (German Science Foundation, DFG) within the Collaborative Research Center SFB1491 and projects 497938371 and 544893192.

Declaration of interests

The authors report no conflict of interest.

REFERENCES

Allmann-Rahn, F., Trost, T. & Grauer, R. 2018 Temperature gradient driven heat flux closure in fluid simulations of collisionless reconnection. *J. Plasma Phys.* **84**, 905840307.

Arrò, G., Califano, F. & Lapenta, G. 2020 Statistical properties of turbulent fluctuations associated with electron-only magnetic reconnection. *Astron. Astrophys.* **642**, A45.

Arrò, G., Califano, F. & Lapenta, G. 2022 Spectral properties and energy transfer at kinetic scales in collisionless plasma turbulence. *Astron. Astrophys.* **668**, A33.

Arrò, G., Pucci, F., Califano, F., Innocenti, M.E. & Lapenta, G. 2023 Generation of subion scale magnetic holes from electron shear flow instabilities in plasma turbulence. *Astrophys. J.* **958**, 11.

Birn, J. & Priest, E.R. 2007 *Reconnection of Magnetic Fields: Magnetohydrodynamics and Collisionless Theory and Observations*, Chap. **3**, pp. 87–166. Cambridge University Press.

Biskamp, D. 2000 *Magnetic Reconnection in Plasmas*, Chap. **2**, pp. 10–29. Cambridge University Press.

Bittencourt, J.A. 2013 *Fundamentals of Plasma Physics*. Springer Science & Business Media.

BURCH, J.L., *et al.* 2016 Electron-scale measurements of magnetic reconnection in space. *Science* **352**, aaf2939.

CALIFANO, F., CERRI, S.S., FAGANELLO, M., LAVEDER, D., SISTI, M. & KUNZ, M.W. 2020 Electron-only reconnection in plasma turbulence. *AIP Conf. Proc.* **8**, 317.

CHEW, G.F., GOLDBERGER, M.L. & LOW, F.E. 1956 The boltzmann equation an d the one-fluid hydromagnetic equations in the absence of particle collisions. *Proc. Royal Soc. Lond. Ser. A. Math. Phys. Sci.*, **236**, 112–118,

EGEDAL, J., FOX, W., KATZ, N., PORKOLAB, M., ØIEROSET, M., LIN, R.P., DAUGHTON, W. & DRAKE, J.F. 2008 Evidence and theory for trapped electrons in guide field magnetotail reconnection. *J. Geophys. Res.: Space Phys.* **113**, A12207.

EGEDAL, J., LE, A. & DAUGHTON, W. 2013 A review of pressure anisotropy caused by electron trapping in collisionless plasma, and its implications for magnetic reconnection. *Phys. Plasmas* **20**.

FRANCI, L., PAPINI, E., MICERA, A., LAPENTA, G., HELLINGER, P., DEL SARTO, D., BURGESS, D. & LANDI, S. 2022 Anisotropic electron heating in turbulence-driven magnetic reconnection in the near-sun solar wind. *Astrophys. J.* **936**, 27.

GAO, C.-H., TANG, B.-B., GUO, X.-C., LI, W.Y., KHOTYAINTSEV, Y.V., GRAHAM, D.B., TURNER, D.L., YANG, Z.W. & WANG, C. 2023 Agyrotropic electron distributions in the terrestrial foreshock transients. *Geophys. Res. Lett.* **50**, e2022GL102235.

GOLDMAN, M.V., NEWMAN, D.L. & LAPENTA, G. 2016 What can we learn about magnetotail reconnection from 2d pic Harris-sheet simulations? *Space Sci. Rev.* **199**, 651–688.

GONZALEZ-HERRERO, D., BOELLA, E. & LAPENTA, G. 2018 Performance analysis and implementation details of the energy conserving semi-implicit method code (ECSIM). *Comput. Phys. Commun.* **229**, 162–169.

GRANIER, C., TASSI, E., LAVEDER, D., PASSOT, T. & SULEM, P.-L. 2024 Influence of ion-to-electron temperature ratio on tearing instability and resulting subion-scale turbulence in a low-βe collisionless plasma. *Phys. Plasmas* **31**.

GUAN, Y., LU, Q., LU, S., HUANG, K. & WANG, R. 2023 Reconnection rate and transition from ion-coupled to electron-only reconnection. *Astrophys. J.* **958**, 172.

GUAN, Y., LU, Q., LU, S., SHU, Y. & WANG, R. 2024 Role of ion dynamics in electron-only magnetic reconnection. *Geophys. Res. Lett.* **51**, e2024GL110787.

GUO, X., HORIUCHI, R., CHENG, C.Z., KAMINOU, Y. & ONO, Y. 2017 Energy conversion mechanism for electron perpendicular energy in high guide-field reconnection. *Phys. Plasmas* **24**, 032901.

GUO, X., INOMOTO, M., SUGAWARA, T., YAMASAKI, K., USHIKI, T., ONO, Y., *et al.* 2015 Localized electron heating by strong guide-field magnetic reconnection. *Phys. Plasmas* **22**, 101201.

HESSE, M. 2006 Dissipation in magnetic reconnection with a guide magnetic field. *Phys. Plasmas* **13**.

HESSE, M. & CASSAK, P.A. 2020 Magnetic reconnection in the space sciences: past, present, and future. *J. Geophys. Res.: Space Phys.* **125**, e2018JA025935.

HESSE, M., KUZNETSOVA, M. & HOSHINO, M. 2002 The structure of the dissipation region for component reconnection: Particle simulations. *Geophys. Res. Lett.* **29**, 4–1.

HESSE, M., SCHINDLER, K., BIRN, J. & KUZNETSOVA, M. 1999 The diffusion region in collisionless magnetic reconnection. *Phys. Plasmas* **6**, 1781–1795.

HORIUCHI, R., USAMI, S. & OHTANI, H. 2014 Influence of a guide field on collisionless driven reconnection. *Plasma Fusion Res.* **9**, 1401092.

HUBBERT, M., RUSSELL, C.T., QI, Y., LU, S., BURCH, J.L., GILES, B.L. & MOORE, T.E. 2022 Electron-only reconnection as a transition phase from quiet magnetotail current sheets to traditional magnetotail reconnection. *J. Geophys. Res.: Space Phys.* **127**, e2021JA029584.

HWANG, K.-J., *et al.* 2019 Electron vorticity indicative of the electron diffusion region of magnetic reconnection. *Geophys. Res. Lett.* **46**, 6287–6296.

INNOCENTI, M.E., GOLDMAN, M., NEWMAN, D., MARKIDIS, S. & LAPENTA, G. 2015 Evidence of magnetic field switch-off in collisionless magnetic reconnection. *Astrophys. J. Lett.* **810**, L19.

JI, H., *et al.* 2023 Laboratory study of collisionless magnetic reconnection. *Space Sci. Rev.* **219**, 76.

KLEVA, R.G., DRAKE, J.F. & WAELBROECK, F.L. 1995 Fast reconnection in high temperature plasmas. *Phys. Plasmas* **2**, 23–34.

LAPENTA, G., *et al.* 2017*a* On the origin of the crescent-shaped distributions observed by MMS at the magnetopause. *J. Geophys. Res.: Space Phys.* **122**, 2024–2039.

LAPENTA, G. 2017 Exactly energy conserving semi-implicit particle in cell formulation. *J. Comput. Phys.* **334**, 349–366.

LAPENTA, G., GOLDMAN, M., NEWMAN, D.L. & ERIKSSON, S. 2022 Formation and reconnection of electron scale current layers in the turbulent outflows of a primary reconnection site. *Astrophys. J.* **940**, 187.

LAPENTA, G., GONZALEZ-HERRERO, D. & BOELLA, E. 2017*b* Multiple-scale kinetic simulations with the energy conserving semi-implicit particle in cell method. *J. Plasma Phys.* **83**, 705830205.

LAPENTA, G., MARKIDIS, S., DIVIN, A., GOLDMAN, M.V. & NEWMAN, D.L. 2011 Bipolar electric field signatures of reconnection separatrices for a hydrogen plasma at realistic guide fields. *Geophys. Res. Lett.* **38**.

LAPENTA, G., MARKIDIS, S., GOLDMAN, M.V. & NEWMAN, D.L. 2015 Secondary reconnection sites in reconnection-generated flux ropes and reconnection fronts. *Nat. Phys.* **11**, 690–695.

LAVRAUD, B., *et al.* 2021 Magnetic reconnection as a mechanism to produce multiple thermal proton populations and beams locally in the solar wind. *Astron. Astrophys.* **656**, A37.

LE, A., EGEDAL, J., OHIA, O., DAUGHTON, W., KARIMABADI, H. & LUKIN, V.S. 2013 Regimes of the electron diffusion region in magnetic reconnection. *Phys. Rev. Lett.* **110**, 135004.

LU, S., *et al.* 2020 Magnetotail reconnection onset caused by electron kinetics with a strong external driver. *Nat. Commun.* **11**, 5049.

LU, Q., HUANG, K., GUAN, Y., LU, S. & WANG, R. 2023 Energy dissipation in magnetic islands formed during magnetic reconnection. *Astrophys. J.* **954**, 146.

LU, S., LU, Q., WANG, R., PRITCHETT, P.L., HUBBERT, M., QI, Y., HUANG, K., LI, X. & RUSSELL, C.T. 2022 Electron-only reconnection as a transition from quiet current sheet to standard reconnection in earth's magnetotail: particle-in-cell simulation and application to mms data. *Geophys. Res. Lett.* **49**, e2022GL098547.

MALLET, A. 2020 The onset of electron-only reconnection. *J. Plasma Phys.* **86**, 905860301.

MARKIDIS, S., LAPENTA, G., DIVIN, A., GOLDMAN, M., NEWMAN, D. & ANDERSSON, L. 2012 Three dimensional density cavities in guide field collisionless magnetic reconnection. *Phys. Plasmas* **19**, 032119.

MCCUBBIN, A.J., HOWES, G.G. & TENBARGE, J.M. 2022 Characterizing velocity–space signatures of electron energization in large-guide-field collisionless magnetic reconnection. *Phys. Plasmas* **29**.

MICERA, A., BOELLA, E., ZHUKOV, A.N., SHAABAN, S.M., LÓPEZ, R.A., LAZAR, M. & LAPENTA, G. 2020 Particle-in-cell simulations of the parallel proton firehose instability influenced by the electron temperature anisotropy in solar wind conditions. *Astrophys. J.* **893**, 130.

MUÑOZ, P.A. & BÜCHNER, J. 2016 Non-maxwellian electron distribution functions due to self-generated turbulence in collisionless guide-field reconnection. *Phys. Plasmas* **23**.

MUÑOZ, P.A., KILIAN, P. & BÜCHNER, J. 2014 Instabilities of collisionless current sheets revisited: the role of anisotropic heating. *Phys. Plasmas* **21**.

NEWMAN, D.L., ERIKSSON, S. & LAPENTA, G. 2022 Tripolar guide magnetic fields due to island coalescence in solar wind current sheets: simulation and theory. *Phys. Plasmas* **29**.

NG, J., EGEDAL, J., LE, A., DAUGHTON, W. & CHEN, L.-J. 2011 Kinetic structure of the electron diffusion region in antiparallel magnetic reconnection. *Phys. Rev. Lett.* **106**, 065002.

NG, J., HUANG, Y.-M., HAKIM, A., BHATTACHARJEE, A., STANIER, A., DAUGHTON, W., WANG, L. & GERMASCHEWSKI, K. 2015 The island coalescence problem: scaling of reconnection in extended fluid models including higher-order moments. *Phys. Plasmas* **22**.

OKA, M., BIRN, J., EGEDAL, J., GUO, F., ERGUN, R.E., TURNER, D.L., KHOTYAINTSEV, Y., HWANG, K.-J., COHEN, I.J. & DRAKE, J.F. 2023 Particle acceleration by magnetic reconnection in geospace. *Space Sci. Rev.* **219**, 75.

PHAN, T.D., *et al.* 2018 Electron magnetic reconnection without ion coupling in earth's turbulent magnetosheath. *Nature* **557**, 202–206.

PRITCHETT, P.L. 2001 Geospace environment modeling magnetic reconnection challenge: simulations with a full particle electromagnetic code. *J. Geophys. Res.: Space Phys.* **106**, 3783–3798.

PRITCHETT, P.L. 2005 Onset and saturation of guide-field magnetic reconnection. *Phys. Plasmas* **12**.

PRITCHETT, P.L. & CORONITI, F.V. 2004 Three-dimensional collisionless magnetic reconnection in the presence of a guide field. *J. Geophys. Res.: Space Phys.* **109**.

PUCCI, F., USAMI, S., JI, H., GUO, X., HORIUCHI, R., OKAMURA, S., FOX, W., JARA-ALMONTE, J., YAMADA, M. & YOO, J. 2018 Energy transfer and electron energization in collisionless magnetic reconnection for different guide-field intensities. *Phys. Plasmas* **25**.

PYAKUREL, P.S., SHAY, M.A., DRAKE, J.F., PHAN, T.D., CASSAK, P.A. & VERNIERO, J.L. 2021 Faster form of electron magnetic reconnection with a finite length x-line. *Phys. Rev. Lett.* **127**, 155101.

REN, J. & LAPENTA, G. 2024 Recent development of fully kinetic particle-in-cell method and its application to fusion plasma instability study. *AIP Conf. Proc.* **12**, 1340736.

RICCI, P., BRACKBILL, J.U., DAUGHTON, W. & LAPENTA, G. 2004 Collisionless magnetic reconnection in the presence of a guide field. *Phys. Plasmas* **11**, 4102–4114.

ROGERS, B.N., DENTON, R.E. & DRAKE, J.F. 2003 Signatures of collisionless magnetic reconnection. *J. Geophys. Res.: Space Phys.* **108**.

ROY, S., BANDYOPADHYAY, R., MATTHAEUS, W.H. & PYAKUREL, P.S. 2024 Energy dissipation in electron-only reconnection. *Astrophys. J.* **964**, 44.

SEPÚLVEDA, M. & ALEJANDRO, P. 2015 Fully kinetic pic simulations of current sheet instabilities for the solar corona, *PhD thesis*. Georg-August-Universität Göttingen.

SHARMA PYAKUREL, P., SHAY, M.A., PHAN, T.D., MATTHAEUS, W.H., DRAKE, J.F., TENBARGE, J.M., HAGGERTY, C.C., KLEIN, K.G., CASSAK, P.A. & Parashar. TN & others 2019 transition from ion-coupled to electron-only reconnection: basic physics and implications for plasma turbulence. *Phys. Plasmas* **26**.

SHAY, M.A., DRAKE, J.F., SWISDAK, M. & ROGERS, B.N. 2004 The scaling of embedded collisionless reconnection. *Phys. Plasmas* **11**, 2199–2213.

SHAY, M.A., PHAN, T.D., HAGGERTY, C.C., FUJIMOTO, M., DRAKE, J.F., MALAKIT, K., CASSAK, P.A. & SWISDAK, M. 2016 Kinetic signatures of the region surrounding the x line in asymmetric (magnetopause) reconnection. *Geophys. Res. Lett.* **43**, 4145–4154.

SHI, P., *et al.* 2021 Alfvénic modes excited by the kink instability in phasma. *Phys. Plasmas* **28**, 032101.

SHI, P., *et al.* 2022b Electron-only reconnection and associated electron heating and acceleration in phasma. *Phys. Plasmas* **29**, 032101.

SHI, P., SCIME, E.E., BARBHUIYA, M.H., CASSAK, P.A., ADHIKARI, S., SWISDAK, M. & STAWARZ, J.E. 2023 Using direct laboratory measurements of electron temperature anisotropy to identify the heating mechanism in electron-only guide field magnetic reconnection. *Phys. Rev. Lett.* **131**, 155101.

SHI, P., SRIVASTAV, P., BARBHUIYA, M.H., CASSAK, P.A., SCIME, E.E. & SWISDAK, M. 2022 Laboratory observations of electron heating *a*nd non-Maxwellian distributions at the kinetic scale during electron-only magnetic reconnection. *Phys. Rev. Lett.* **128**, 025002.

SHUSTER, J.R., CHEN, L.-J., HESSE, M., ARGALL, M.R., DAUGHTON, W., TORBERT, R.B. & BESSHO, N. 2015 Spatiotemporal evolution of electron characteristics in the electron diffusion region of magnetic reconnection: implications for acceleration and heating. *Geophys. Res. Lett.* **42**, 2586–2593.

SNYDER, P.Y 9B., HAMMETT, G.W. & DORLAND, W. 1997 Landau fluid models of collisionless magnetohydrodynamics. *Phys. Plasmas* **4**, 3974–3985.

STANIER, A., DAUGHTON, W., SIMAKOV, A.N., CHACON, L., LE, A., KARIMABADI, H., NG, J. & BHATTACHARJEE, A. 2017 The role of guide field in magnetic reconnection driven by island coalescence. *Phys. Plasmas* **24**, 022124.

STANIER, A., SIMAKOV, A.N., CHACON, L. & DAUGHTON, W. 2015*a* Fast magnetic reconnection with large guide fields. *Phys. Plasmas* **22**, 010701.

STANIER, A., SIMAKOV, A.N., CHACÓN, L. & DAUGHTON, W. 2015*b* Fluid vs. kinetic magnetic reconnection with strong guide fields. *Phys. Plasmas* **22**, 101203.

STAWARZ, J.E., *et al.* 2019 Properties of the turbulence associated with electron-only magnetic reconnection in earth's magnetosheath. *Astrophys. J. Lett.* **877**, L37.

STAWARZ, J.E., EASTWOOD, J.P., PHAN, T.D., GINGELL, I.L., PYAKUREL, P.S., SHAY, M.A., ROBERTSON, S.L., RUSSELL, C.T. & LE CONTEL, O. 2022 Turbulence-driven magnetic reconnection and the magnetic correlation length: observations from magnetospheric multiscale in earth's magnetosheath. *Phys. Plasmas* **29**, 012302.

SWISDAK, M. 2016 Quantifying gyrotropy in magnetic reconnection. *Geophys. Res. Lett.* **43**, 43–49.

SWISDAK, M., DRAKE, J.F., SHAY, M.A. & MCILHARGEY, J.G. 2005 Transition from antiparallel to component magnetic reconnection. *J. Geophys. Res.: Space Phys.* **110**, A05210.

WAN, W. & LAPENTA, G. 2008 Evolutions of non-steady-state magnetic reconnection. *Phys. Plasmas* **15**, 102302.

WETHERTON, B.A., EGEDAL, J., LE, A. & DAUGHTON, W. 2021 Anisotropic electron fluid closure validated by in situ spacecraft observations in the far exhaust of guide-field reconnection. *J. Geophys. Res.: Space Phys.* **126**, e2020JA028604.

WETHERTON, B.A., EGEDAL, J., LÊ, A. & DAUGHTON, W. 2019 Validation of anisotropic electron fluid closure through in situ spacecraft observations of magnetic reconnection. *Geophys. Res. Lett.* **46**, 6223–6229.

WHEALTON, J.H. & WOO, S.-B. 1972 Ion velocity distribution of a weakly ionized gas in a uniform electric field of arbitrary strength. *Phys. Rev. A* **6**, 2319–2325.

WILSON, F., NEUKIRCH, T., HESSE, M., HARRISON, M.G. & STARK, C.R. 2016 Particle-in-cell simulations of collisionless magnetic reconnection with a non-uniform guide field. *Phys. Plasmas* **23**, 032302.

XIONG, Q.Y., HUANG, S.Y., ZHANG, J., YUAN, Z.G., JIANG, K., WU, H.H., LIN, R.T., YU, L. & TANG, Y.T. 2024 Guide field dependence of energy conversion and magnetic topologies in reconnection turbulent outflow. *Geophys. Res. Lett.* **51**, e2024GL109356.

YANG, Y., MATTHAEUS, W.H., PARASHAR, T.N., HAGGERTY, C.C., ROYTERSHTEYN, V., DAUGHTON, W., WAN, M., SHI, Y. & CHEN, S. 2017b Energy transfer, pressure tensor, and heating of kinetic plasma. *Phys. Plasmas* **24**, 072306.

YANG, Y., MATTHAEUS, W.H., PARASHAR, T.N., WU, P., WAN, M., SHI, Y., CHEN, S., ROYTERSHTEYN, V. & DAUGHTON, W. 2017a Energy transfer channels *a*nd turbulence cascade in vlasov-maxwell turbulence. *Phys. Rev. E* **95**, 061201.

YI, Y., ZHOU, M., SONG, L. & DENG, X. 2020 Energy conversion during multiple x-lines reconnection. *Phys. Plasmas* **27**, 122905.

ZELENYI, L.M. & KRASNOSELSKIKH, V.V. 1979 Relativistic modes of tearing instability in a background plasma. *Soviet Astron.* **23**, 460, 1979.

ZHONG, Z.H., ZHOU, M., DENG, X.H., SONG, L.J., GRAHAM, D.B., TANG, R.X., MAN, H.Y., PANG, Y., KHOTYAINTSEV, Y.V. & GILES, B.L. 2021 Three-dimensional electron-scale magnetic reconnection in earth's magnetosphere. *Geophys. Res. Lett.* **48**, 2020GL090946.

ZHOU, M., DENG, X.H., ZHONG, Z.H., PANG, Y., TANG, R.X., EL-ALAOUI, M., WALKER, R.J., RUSSELL, C.T., LAPENTA, G. & R.J.,STRANGEWAY *et al.* 2019 Observations of an electron diffusion region in symmetric reconnection with weak guide field. *Astrophys. J.* **870**, 34.

ZWEIBEL, E.G. & YAMADA, M. 2009 Magnetic reconnection in astrophysical and laboratory plasmas. *Annu. Rev. Astron. Astr.* **47**, 291–332.